Journal of Manufacturing Processes 105 (2023) 359–369

Contents lists available at ScienceDirect

Journal of Manufacturing Processes

journal homepage: www.elsevier.com/locate/manpro

Ultrasonic effects with different vibration positions on gas tungsten arc wire additive manufactured aluminum nanocomposite

Tianzhao Wang, Xun Liu *, Mason Darnell

Welding Engineering Program, Department of Materials Science and Engineering, The Ohio State University, 1248 Arthur Adams Drive, Columbus, OH 43221, United States

ARTICLE INFO

Keywords:
Wire arc additive manufacturing
Power ultrasound
Metal matrix nanocomposite
Grain orientation
Nanoparticles

ABSTRACT

Ultrasonically assisted gas tungsten arc based wire additive manufacturing (UA-GTAAM) of TiB_2 nanoparticle-reinforced AA7075 aluminum metal matrix nanocomposite (MMNC) was conducted with the UA probe directly immersed in the molten pool. This work focuses on the UA effects with different probe positions on the UA-melt interactions and the resulting microstructure. In situ high-speed imaging reveals melt pool surface ripples induced by UA. More refined surface ripples, corresponding to a faster melt flow, are observed with the UA probe immersed deeper into the melt. This condition also leads to a lighter etched color under optical microscope, which is related to a more homogeneous microstructure with less eutectic phase at grain boundaries. Electron backscatter diffraction (EBSD) analysis was employed for grain orientation and nanoparticle distributions, where the lower Confidence Index (CI) served as an indicator for intragranular nanoparticle segregation. The EBSD results show a strong (110) texture in the conventional WAAM builds. High-resolution backscattered electron (BSE) imaging reveals nanoparticles tend to segregate into preferred (001) and (111) grains. UA suppresses the epitaxial growth of (110) grains and promotes a more randomly orientated microstructure. Accordingly, more (001) and (111) grains are available to accommodate nanoparticles and promote a more homogeneous dispersion.

1. Introduction

Ultrasonic (UA) melt treatment has been applied to molten metal processes due to its efficacy in melt degassing, microstructure refinement, and de-agglomeration [1,2]. Ultrasonic melt treatment (UST) relies on the UA-melt interactions, including ***acoustic cavitation, acoustic streaming, and ultrasonic capillary effect***. An ultrasound-eroded melt undergoes an alternating positive and negative pressure field. Under negative pressure, the gaseous phase (hydrogen in the case of Al melt) is forced to diffuse out as gas bubbles [3]. The gas bubbles get compressed during the positive pressure phase. The alternating expansion and compression phases induce the pulsation of gas bubbles, resulting in a rectified diffusion of hydrogen from the melt into the gas bubbles and accordingly bubble growth [4]. On the other hand, the compression pressure can also cause bubble collapse, resulting in the release of shockwaves with high pressure and temperature. In addition, liquid microjets are generated upon the implosive bubble collapse with a velocity in the range of 100 m/s [2,5]. The process of bubble formation, pulsation, and collapse driven by ultrasound is called ***acoustic cavitation***. The hydrodynamic flows driven by UA vibration, known as ***acoustic streaming***, can reach velocities of a few meters per second, leading to mixing and stirring effects in the melt [2]. Upon bubble collapse during acoustic cavitation, an abnormal liquid penetration into narrow micro-channels can be observed. The pulsation and collapse of cavitation bubbles near the capillary entry generates excessive pressure that surpasses the capillary pressure and thereby promotes deeper and faster liquid penetration into the micro-channels. This phenomenon is known as the ***ultrasonic capillary effect*** [6].

All three UA-melt interactions exhibit synergistic effects that are crucial in UST applications. Ultrasonic degassing is employed to reduce the porosities in the melt [7,8], during which the hydrogen bubbles nucleate at the non-wettable particles in the melt and grow via the rectified hydrogen diffusion driven by acoustic cavitation. When the bubbles reach a critical size, they could rise to the melt surface and escape, which is also aided by acoustic streaming [4,9]. Ultrasonic grain refinement is attributed to several mechanisms, including the ultrasonic impact on the local thermodynamic equilibrium, enhanced heterogeneous nucleation, and primary dendrite fragmentation. The collapse of

* Corresponding author.
E-mail address: liu.7054@osu.edu (X. Liu).

https://doi.org/10.1016/j.jmapro.2023.09.043
Received 20 July 2023; Received in revised form 30 August 2023; Accepted 15 September 2023
Available online 27 September 2023

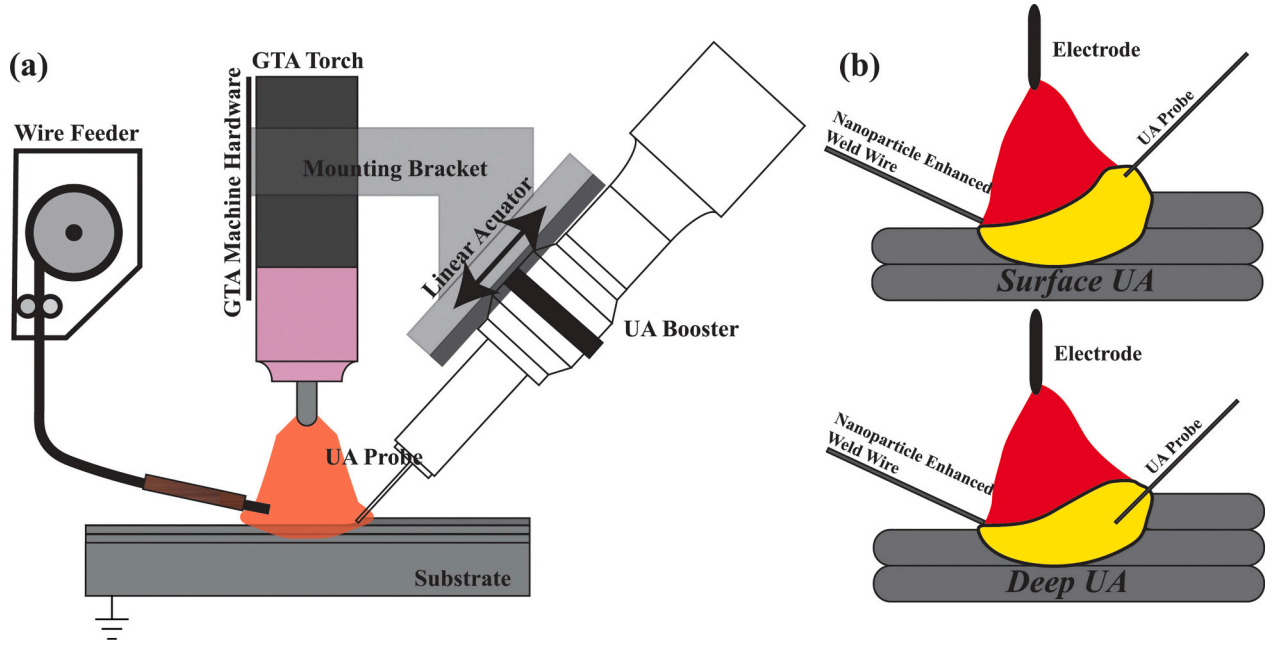

Fig. 1. Schematic illustration of a) UA-GMAAM setup and b) UA probe inserting position.

bubbles during acoustic cavitation produces local high pressure, which increases the melting point of the material and subsequently enhances the degree of undercooling [10,11]. Acoustic cavitation also promotes heterogenous nucleation by improving the wettability of inoculated particles [12,13]. In addition, both acoustic cavitation and streaming contribute to the fragmentation of primary dendrites. These fragments can be conveyed by the acoustic streaming flows back into the melt, where they serve as nucleation sites [14]. UST has been widely applied in the fabrication of metal matrix composite (MMC) [15,16] and metal matrix nanocomposite (MMNC) [17,18] based on its de-agglomerating effect. MMNC shows superior properties over MMC due to the smaller size of reinforcing particles, which helps to avoid stress concentration and to maintain ductility with enhanced strengthening effects [17,18]. However, nanoparticles in MMNC are more susceptible to agglomeration. The smaller particle size results in a higher surface area-to-volume ratio, which in turn increases the interfacial energy and leads to the nanoparticles clustering issue in MMNC systems [15]. Acoustic streaming induced better mixing and stirring in the melt, which promotes better dispersion of nanoparticles in the MMNC melt. Besides, UST is also effective in improving the wettability of particles [2,12,15], thereby reducing the propensity for clustering. Furthermore, ultrasonic capillary effect promotes the penetration of liquid into the microchannels within the particle agglomerations, which can effectively separate the clustered particles [19].

Compared with conventional molten metal processes, additive manufacturing (AM) process usually undergoes rapid solidification with high cooling rate and repeated thermal cycles [20]. Besides, dynamic solid boundaries in AM processes differ from the static solid walls in conventional UST processes, adding more complex ultrasound-induced melt flow. Among different AM processes, wire arc additive manufacturing (WAAM) is advantageous in rapid prototyping at a large scale with low cost and high deposition rate [21]. Limited studies of UST on AM or WAAM of MMNC have been performed, which involves multiple interactions between UA, rapid solidification, and nanoparticles. A transition from coarse columnar to refined equiaxed grain structures was achieved in an AM process of Ti-6Al-4 V alloy by applying UA vibrating to the substrate [22]. A similar approach was also taken in an UA-WAAM process of Inconel alloy, which achieves grain refinement and improved mechanical properties [23]. In our previous works, an ultrasonically assisted Gas Tungsten Arc based wire additive manufacturing (UA-GTAAM) process is developed, where the UA probe was directly immersed in the molten pool with vibration continuously applied throughout multiple layers [24,25]. This has distinctly different ultrasonic propagation paths and thereby UA-melt interaction mechanisms from literature. When UA is applied on the substrate, the vibration propagates from the solid with high acoustic impedance to the liquid with low acoustic impedance [2]. UA attenuation coefficient is proportional to the solid fraction in a solid-liquid mixture system [26]. A large portion of the UA energy is dissipated during the propagation through the substrate. In contrast, when the UA probe is immersed in the melt pool, the acoustic wave propagates through the liquid melt where acoustic impedance is lower than the substrate. In our previous works, the UA-GTAAM process exhibits reduced nanoparticle clusters at grain boundaries, which indicates a better dispersion [24,25]. Different from the intergranular nanoparticle clusters along the grain boundaries, the characterization of intragranular dispersion of nanoparticles in MMNC typically demands the application of high spatial resolution techniques such as transmission electron microscopy (TEM) [27,28]. However, the field of view of TEM is confined to a limited small area typically less than 100 nm [29]. Therefore, a tool capable of characterizing the overall nanoparticle distribution over a broader region is desired for a more statistical understanding.

This study applied a high deposition rate during the UA-GTAAM process, which formed a large molten pool and the UA-melt interactions vary with different UA probing positions. If the probe contacts the upper region of the melt pool, free metal flow coupled with higher melt temperature and reduced viscosity can be expected. On the other hand, submerging the probe deeper into the bottom of the melt pool, where dendritic structure develops, leads to more complicated UA-melt interactions due to the high viscosity and substantial attenuation of UA energy within the mushy zone [2]. In-situ high-speed imaging of the UA-GTAAM is performed to directly observe the UA-melt pool interaction dynamics. The intragranular dispersion of nanoparticles is characterized based on EBSD maps, where the lower confidence index (CI) pixels serve as an indicator for the presence of intragranular nanoparticles segregations.

Table 1
Process parameters of UA-WAAM process.

Pass no.	Voltage/ (V)	Current/ (A)	UA status	Travel speed/ (IPM)	Wire feed speed/(IPM)
1	17	300	OFF	3	105
2		250	OFF		
3–5		200	OFF		
6		200	OFF/ surface/ deep		

2. Materials and experimental methods

2.1. Materials

In this study, an AA7075 alloy reinforced with TiB_2 nanoparticles weld wire was utilized. The weld wire had a diameter of 1.2 mm and consisted of 1.7 vol% TiB2 particles with an ideal diameter ranging from 40 to 60 nm. The fabrication process of the weld wire involved a flux-assisted liquid state incorporation method followed by hot-extrusion [30]. The WAAM build was deposited on a ¾ inch thick AA2219 base plate.

2.2. UA-WAAM process

Fig. 1(a) shows the schematic illustration of the UA-WAAM setup, which is adapted from a conventional GTAW system. The heat source is generated by a non-consumable tungsten electrode. The electrode travels at 3IPM, while the UA probe travels at the same speed behind. An AC pulse waveform with a frequency of 70 Hz is applied during the process. Waveform details were provided in our previous study [24]. The weld wire was fed in front of the electrode with a wire feed speed of 105IPM. The deposition rate, calculated as the ratio between wire feed speed and travel speed, is set at 35, which is significantly higher than the previous range of 5–20 [24,25]. Argon shielding gas with a flow rate of 9.5 L/min is applied throughout the entire building process.

Table 1 shows the process parameters of the UA-WAAM. Five layers were first deposited on the base plate, followed by different UA conditions in the very last pass. The current was set higher in the initial two passes to ensure better wetting of the deposition layer to the base metal. The current was then assigned at 200 A as the steady state. In the last deposition layer, the UA probe was not inserted into the molten pool for the first 15 s, providing a controlled segment designated as No UA. After 15 s, the UA probe was placed on the top surface of the molten pool and traveled together with the arc for 20s, designated as Surface UA. The UA probe was then further immersed into the molten puddle with a depth of 5 mm and traveled for another 20s, designated as Deep UA. The UA probe positions at Surface UA and Deep UA conditions are illustrated in Fig. 1(b). An ultrasonic power percentage of 60 % corresponding to a peak-to-peak vibration amplitude of 20.7 μm was applied.

2.3. High speed imaging of the molten pool

A high-speed camera (Photon SA-X2) with a darkening filter lens was employed for directly observing the molten pool during the last layer deposition. High-speed imaging was performed under natural light. The frame rate was set at 4000fps with a spatial resolution of 1200 × 1200.

2.4. Microstructure characterization

Metallurgical samples were prepared on the transverse cross-section of the build, followed by the standard grinding and polishing procedure. Polished samples were etched with Keller's reagent for 10s to reveal the grain boundaries. Grain size distribution and grain morphology were processed and analyzed using the Mipar software. Scanning electron microscopy (SEM), electron backscatter diffraction (EBSD) and high-resolution backscatter secondary electron (BSE) techniques were performed to characterize grain orientation and nanoparticle dispersion.

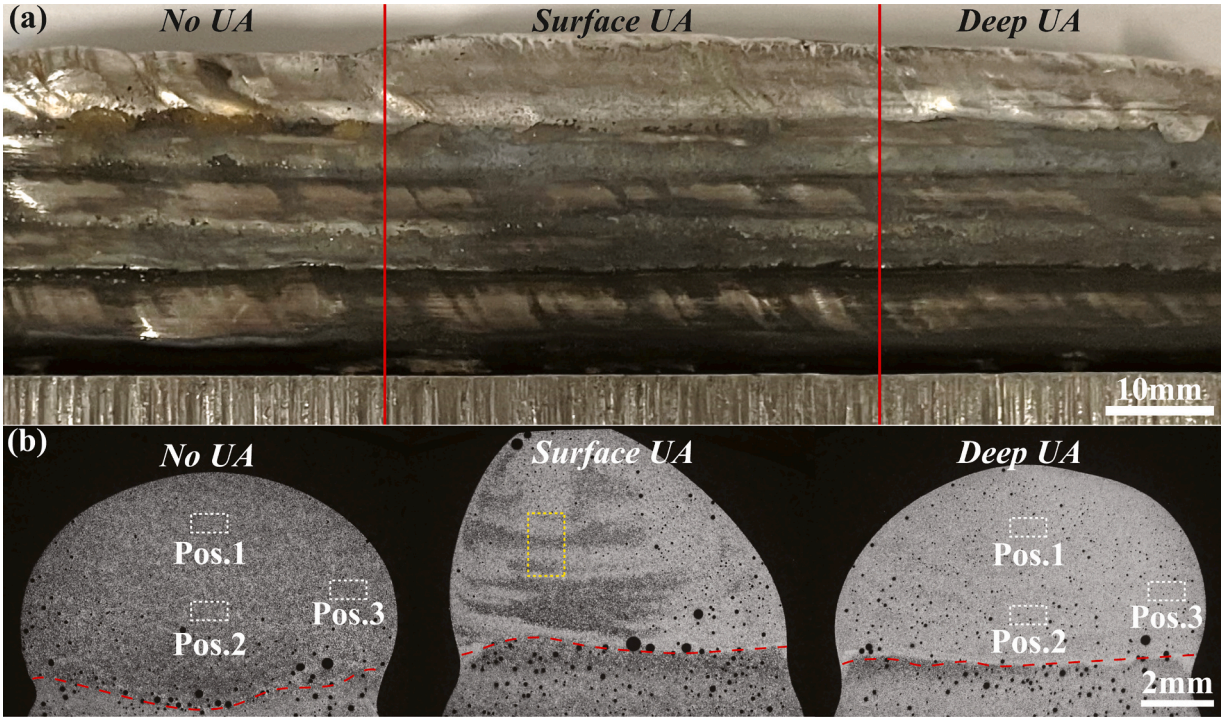

Fig. 2. (a) Side view of UA-WAAM build with varying UA probe positions at different segments (b) the transverse cross-section of the very top bead with different UA probe positions. Locations for EBSD maps were indicated by a white box.

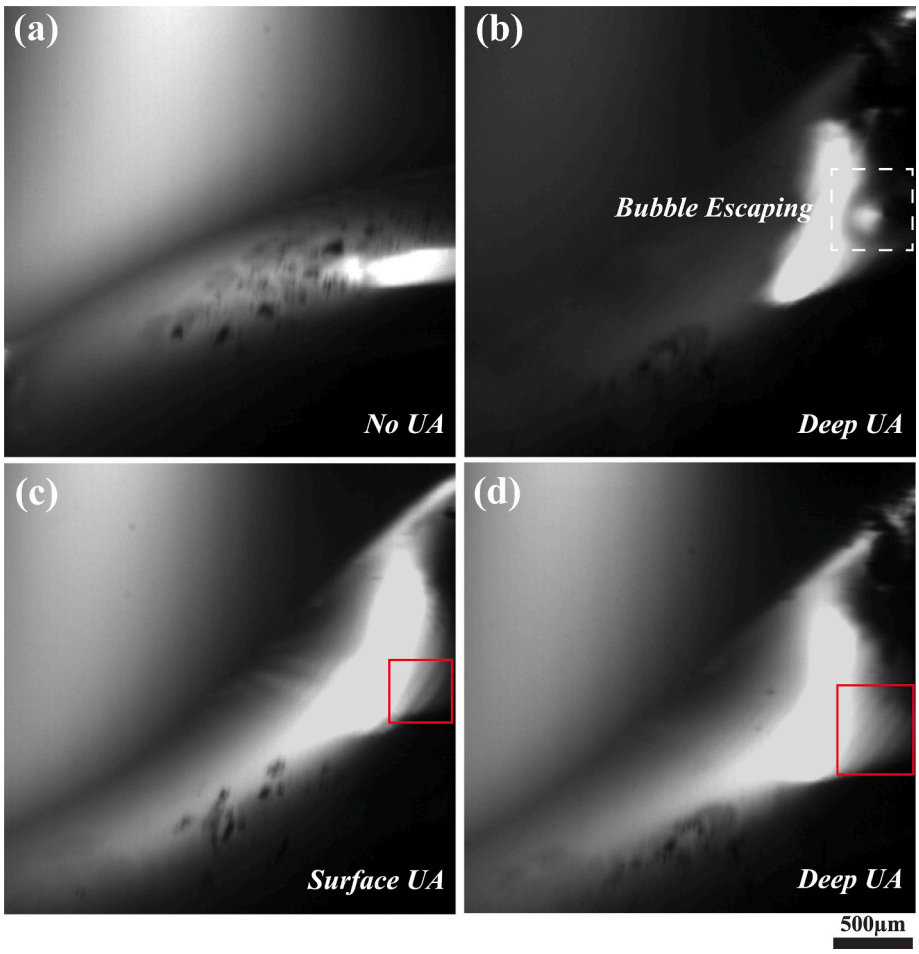

Fig. 3. High-speed images of (a) no UA, (b) deep UA showing a gas bubble escaping the molten pool, (c) surface UA, and (d) deep UA. The red box marks surface ripples on the melt pool induced by ultrasonic vibration. (For interpretation of the references to color in this figure legend, the reader is referred to the web version of this article.)

3. Results and discussions

Fig. 2(a) shows the side view of the WAAM build. Due to the high deposition rate, higher layer heights were observed compared with previous works [24,25]. Layer heights of around 5.7 mm/layer, 5.25 mm/layer, and 5.3 mm/layer were obtained in the case of Surface UA, Deep UA, and No UA respectively, which greatly exceeded the average 1.5 mm/layer and 2.3 mm/layer in our previous works. Based on the sideview of the build as shown in Fig. 2(a), once the UA probe was inserted, an increase in building height was observed. The building height then slightly decreased when the probe was immersed deeper. From the cross-sectional view in Fig. 2(b), a steeple feature was found in the very top bead in the case of Surface UA, which was consistent with our previous observations [24]. This type of geometry is due to the intermolecular adhesive forces between the UA probe and the melt. The adhesive forces provide a lifting effect of the melt and constrict it from falling to the sides. In contrast, the Deep UA does not show any steeple features on the top.

In situ high-speed images of the molten pool at different UA conditions are compared in Fig. 3. Both Surface UA and Deep UA show a significant surface lifting effect around the UA probe. Since the UA probe is far from the molten pool center in the Surface UA case, the lifted molten pool can preserve the steeple shape from collapse due to the high viscosity of the colder melt. In the Deep UA condition, the probe position is closer to the molten pool center. The melt around the probe has higher temperature and fluidity. Accordingly, the lifted melt can freely fall back after the UA probe passes by. Therefore, the steeple feature was not formed in Deep UA case.

In the No UA condition, a smooth molten pool was observed, as shown in Fig. 3(a). In contrast, Surface UA and Deep UA showed closely packed ripples on the melt surface, indicating turbulence and fast flow in the melt [31]. The surface ripples in the case of Deep UA are more refined than the Surface UA condition, as highlighted by the red box in Fig. 3(c) and (d), indicating a more stimulated melt flow. Besides, a gas bubble escaping the molten pool was spotted in Fig. 3(b). This shows the occurrence of UA degassing. The process of UA degassing starts with the cavitation of the dissolved hydrogen, which will increase the number of small pores in the beginning, followed by hydrogen rectified diffusion and growth of bubbles. Eventually, after reaching a critical size, the bubbles float to the top of the melt and escape. However, both UA conditions show more porosities than conventional WAAM deposit, which is opposite to previous observations [24,25]. This indicates that the UA degassing is incomplete in this study, which is possibly caused by the higher deposition rate, i.e. the ratio of wire feed speed over travel speed, of 35 compared with previous studies of 5–20 [24,25]. The higher material deposition rate introduces a longer and deeper molten pool, which requires a higher amount of ultrasonic energy to degas the whole melt.

Fig. 2(b) shows the etched microstructures from different UA conditions. The etched color in the No UA sample is significantly darker than the Deep UA one. The Surface UA sample contains a combination of dark and light etched patterns as marked by the yellow box in Fig. 2(b), which resembles the melt flow streamlines in Fig. 3. Detailed grain size distributions of the top bead from different UA conditions are compared

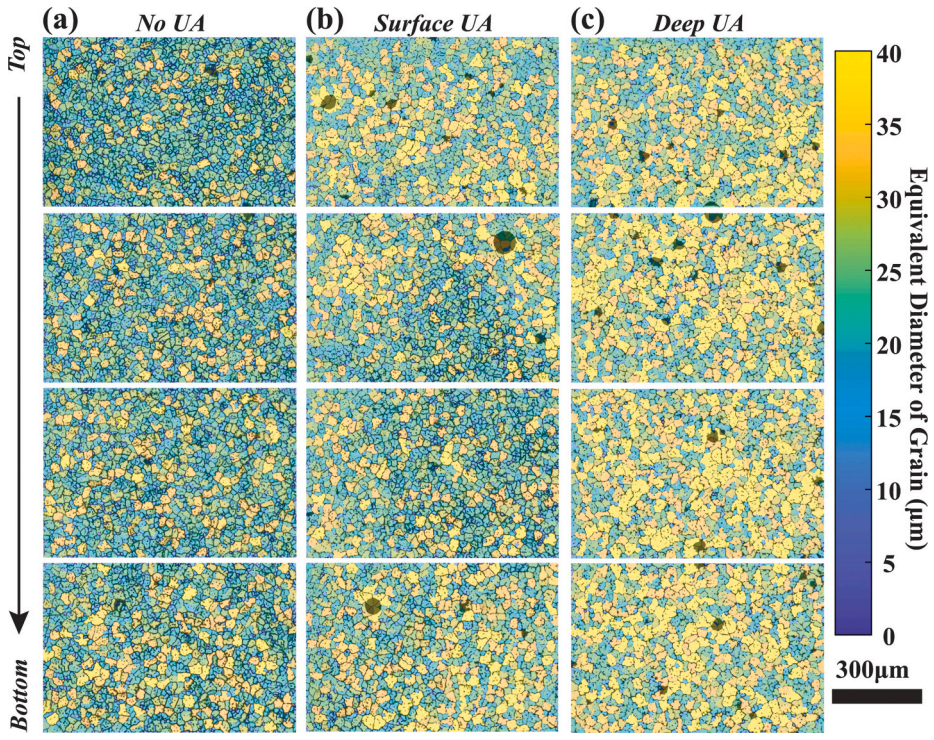

Fig. 4. Grain size distribution in the top bead region of (a) no UA, (b) surface UA, and (c) deep UA samples.

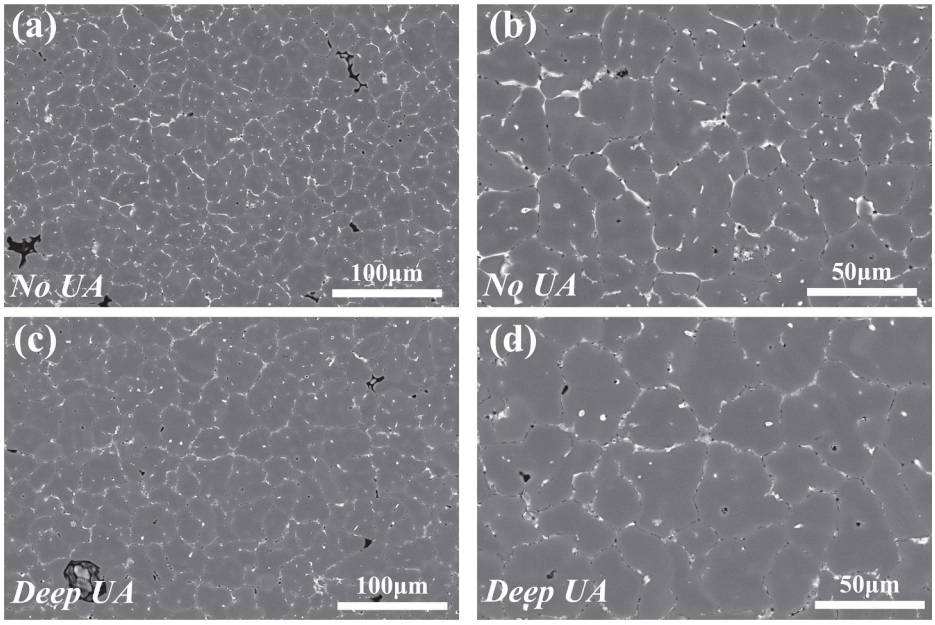

Fig. 5. Backscatter electron (BSE) images of (a & b) no UA and (c & d) deep UA samples.

in Fig. 4. Larger grains are observed in the Deep UA condition than No UA case, as shown in Fig. 4(a & c), which relates to the lighter etched optical macrograph. Meanwhile, the Surface UA sample contains a bimodal grain size distribution as in Fig. 4(b), where refined grains correspond to the dark etched streaks while the coarse grains correspond to the light etched region. In addition to the grain size, the distribution of eutectic phases also affects the etching response. Backscattered electron (BSE) imaging was conducted for No UA and Deep UA samples and shown in Fig. 5. The Deep UA sample exhibits fewer eutectic phases at the grain boundaries than the No UA case, which matches with the lighter etched response.

In the current study, all conditions exhibit equiaxed grain structures, as shown in Fig. 4. This differs from conventional aluminum alloy builds by WAAM, which typically form large columnar dendrites [32]. This phenomenon can be attributed to nanoparticles, which thoroughly modify the solidification process [33]. The nanoparticles decelerate the growth of large columnar dendritic structures and provide heterogeneous nucleation sites in the melt [27]. UA induced microstructure refinement is mainly due to enhanced heterogeneous nucleation and dendrite fragmentation [11]. Due to the substantial presence of nanoparticles serving as heterogeneous nuclei, UA refining effects on MMNC is less pronounced than that of conventional alloys. According to [13],

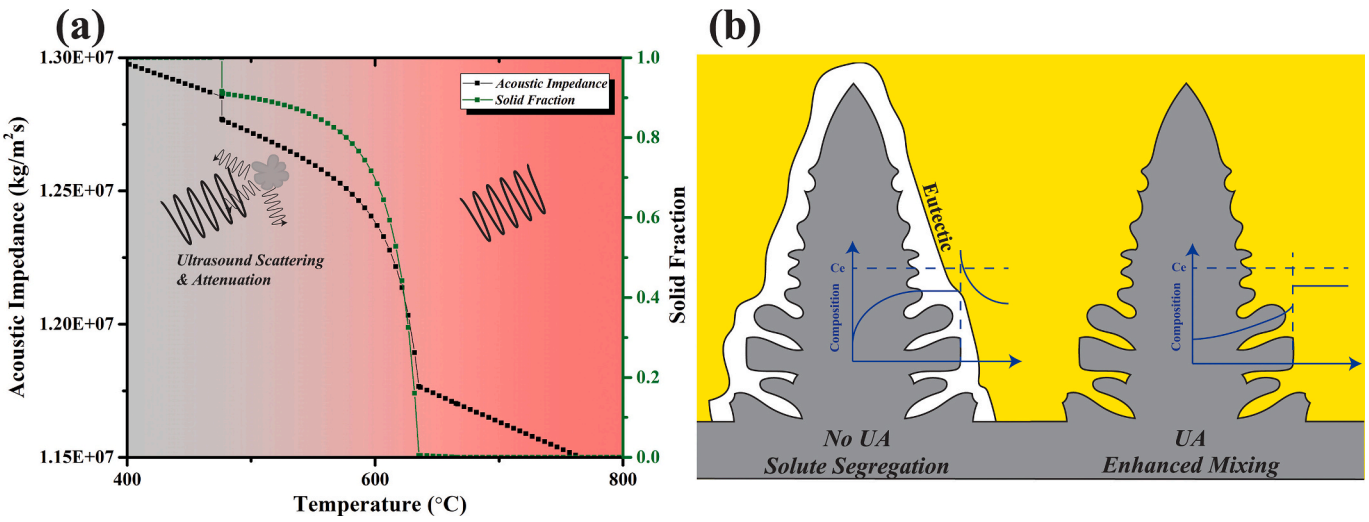

Fig. 6. (a) Acoustic impedance and solid fraction during solidification of AA7075 and (b) schematic illustration of the regular and UA treated solidification process.

cooling curves of Al-Cu alloy show comparable nucleation temperatures between treatments of UA and UA with inoculation particles. In addition, the larger molten pool associated with a high deposition rate leads to lower energy density deposited into the material. An energy density of 2.4 MJ/lb. was applied in current work compared to the 3.7–5.5 MJ/lb. from previous studies [24,25]. Since the input energy will transform into thermal energy in the molten pool and the molten pool boundary is at the solidus temperature, a lower temperature gradient and accordingly wider mushy zone can be expected under the higher deposition rate. The presence of mushy zone in the melt affects ultrasound propagation. Acoustic impedance describes the resistance encountered by the acoustic waves as they propagate [34]:

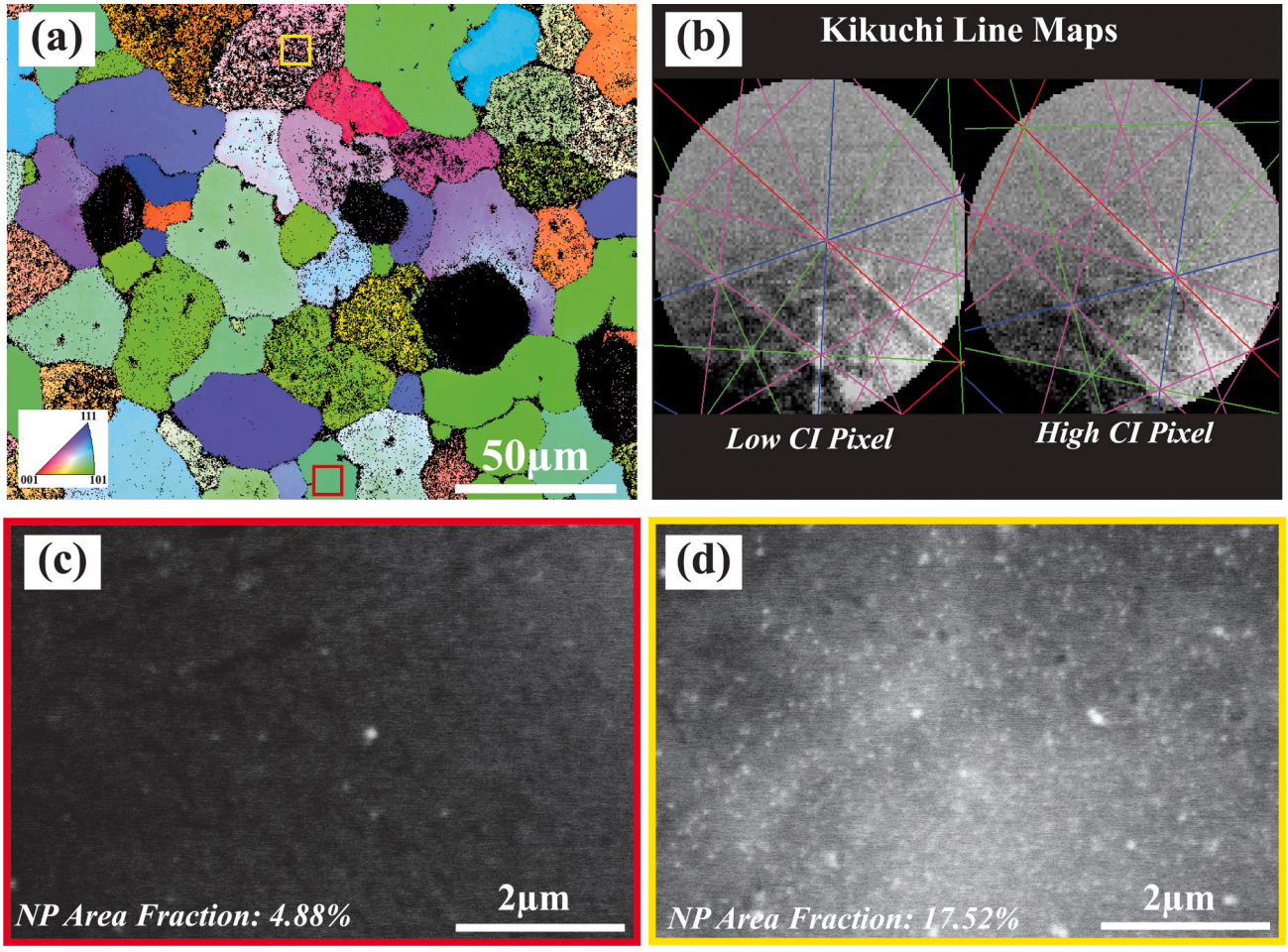

Fig. 7. EBSD images showing (a) IPF and (b) Kikuchi Line Maps, and high-resolution BSE images of a (c) high CI grain indicated by red box and (d) low CI grain indicated by yellow box. (For interpretation of the references to color in this figure legend, the reader is referred to the web version of this article.)

$$Z = \frac{P}{v} = \frac{P}{2\pi fA} = \rho c$$

where P is the acoustic pressure, v is the velocity of the oscillation, f is the frequency of ultrasound, A is the oscillation amplitude, c is the speed of sound in the medium, and ρ is the medium density. During solidification, the medium density and speed of sound exhibit changes as a function of temperature and solid fraction. Therefore, the melt exhibits different acoustic impedances between the mushy zone and the liquid phase. Fig. 6 (a) shows the acoustic impedance and solid fraction during the solidification of AA7075 at different temperatures. Densities and solid fractions of AA7075 were calculated using the thermodynamic simulation program JMatPro. Speed of sound in the melt was calculated based on an empirical equation [2]:

$$c = 4730 - 0.16(T - T_m)$$

where T_m is the melting point in Kelvin. A higher acoustic impedance with larger solid fraction indicates an increased resistance to the ultrasound propagation in the mushy zone. Besides, the dendrites in the mushy zone have smaller sizes than the ultrasonic wavelength in molten aluminum (which is calculated to be 0.23 m based on the speed of sound and frequency) and irregular shapes, which make them strong scattering sites for ultrasound [35]. Therefore, UA energy experiences significant attenuation in the mushy zone due to high impedance and scattering, which limits the dendrite fragmentation effect. Moreover, the attenuated UA energy transforms into thermal energy and promotes grain growth instead. Similar results were described in [36]: the semi-solid Al-Cu alloy with a 25 % solid fraction isothermally treated with UA showed coarsened grains, which was due to the limited UA fragmentation and grain growth caused by additional UA energy input [37].

Moreover, acoustic streaming and cavitation induce the redistribution of solute elements and nanoparticles at the solid-liquid (S-L) interface. Fig. 6(b) illustrates the solidification process highlighting the nucleation of eutectic phases at the grain boundaries in No UA and UA conditions. During regular solidification, solutes are rejected to melt at the S-L interface. The segregated solutes at the S-L interface will eventually reach the eutectic composition and halt crystal growth by forming eutectic phases at grain boundaries. Under UA treatment, the acoustic streaming and cavitation effect will enhance the mixing of solutes through stimulated convection flows in the melt, reducing the element segregation at the S-L interface. Accordingly, delayed nucleation of eutectic phases will slow down the process of grain boundary formation, resulting in larger grain sizes and more homogeneous microstructure. However, it should be noted the grain coarsening under UA observed in this study is not caused by a single mechanism and needs further in situ studies for direct evidence to support these hypotheses.

Inverse pole figure (IPF) and kernel average misorientation (KAM) maps were constructed from raw EBSD analysis results without post-process clean-ups. The confidence index (CI) calculates the fitness of matched Kikuchi patterns among possible solutions, defined as [38]:

$$CI = (V_I - V_{II}/V_{Ideal})$$

where V_I and V_{II} are the largest and second largest number of votes for an orientation solution and V_{Ideal} is the total number of possible triplets of Kikuchi bands. The lower CI values are caused by interferences of Kikuchi bands, which introduce artifacts of the solution votes. Considering the TiB_2 nanoparticle in the weld wire, nanoparticle segregations within the grain would interfere with the Kikuchi bands. In a recent study of additive manufacturing of AA7075 MMNC, Transmission EBSD (TEBSD) analyzed grain maps showed unindexed (low CI) pixels in several grains, which were observed to contain significant amount of nanoparticles within these grains through TEM [28]. Fig. 7(a) shows a representative EBSD map in the Surface UA sample in this study. Low CI pixels can be observed in certain grains, however, these pixels do not encompass the entire map, which is in accordance with grain maps from

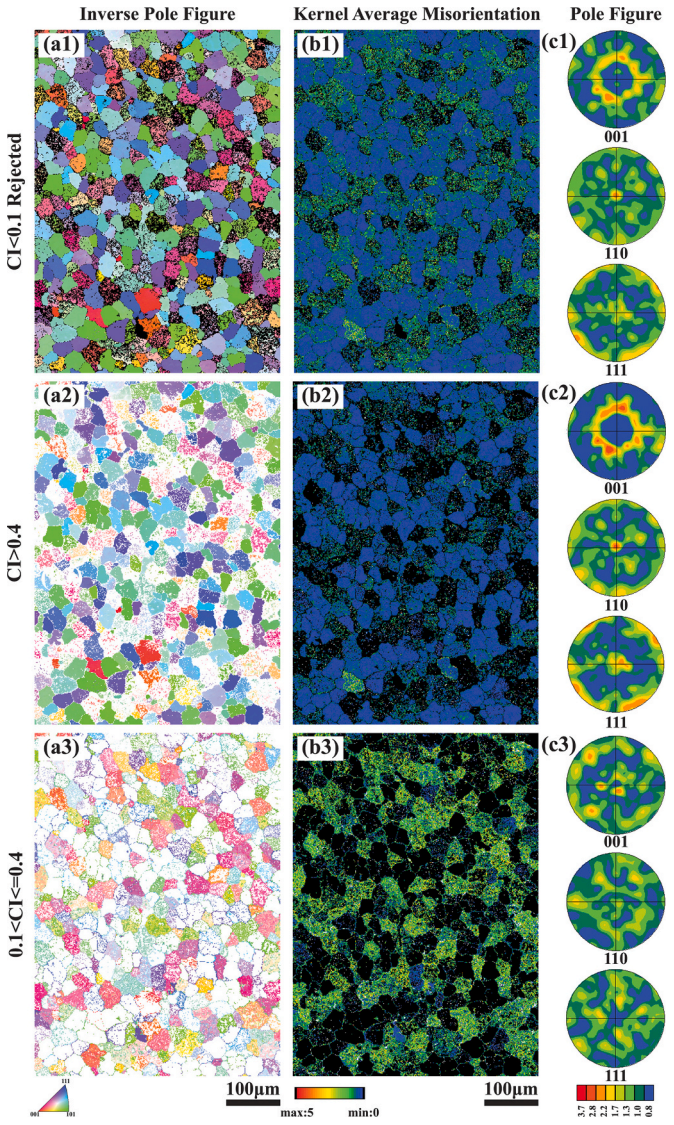

Fig. 8. The (a1) IPF map, (b1) KAM map, and (c1) pole figs. (PF) of the scanned data with CI values lower than 0.1 rejected; the (a2) IPF map, (b2) KAM map, and (c2) PF of the scanned data with high CI values higher than 0.4; the (a3) IPF map, (b3) KAM map, and (c3)PF of the scanned data with lower CI values higher than 0.1 but no larger than 0.4.

TEBSD analysis by Lin et al. [28]. The Kikuchi line maps of pixels with high and low CI values in the same grain are shown in Fig. 7(b). By comparing two pixels, the Kikuchi Line Map of the low CI pixel shows an overlaid Kikuchi pattern, consisting of the pattern of aluminum matrix (identical to high CI Kikuchi bands) and a secondary Kikuchi pattern which is likely caused by electron beam interacting with TiB_2 nanoparticle lattice. The interfered Kikuchi pattern affects the votes for solutions and results in a low CI value.

High-resolution BSE imaging was performed to analyze the nanoparticle distribution in both high and relatively lower CI grains. One high CI grain and one lower CI grain were selected for analysis, marked by the red and yellow boxes, respectively, in Fig. 7(a). The results are shown in Fig. 7(c) and (d), respectively. The white spots in the BSE images correspond to nanoparticles, which have a higher *Z*-contrast compared to the surrounding matrix. Area fractions of nanoparticles in lower CI and high CI grains are calculated as around 17 % and 5 %, respectively. Considering only an average of 1.7 vol% nanoparticles in the weld wire, the fraction of nanoparticles in the lower CI grain is uncommonly high. Besides, several large white spots can be noticed in

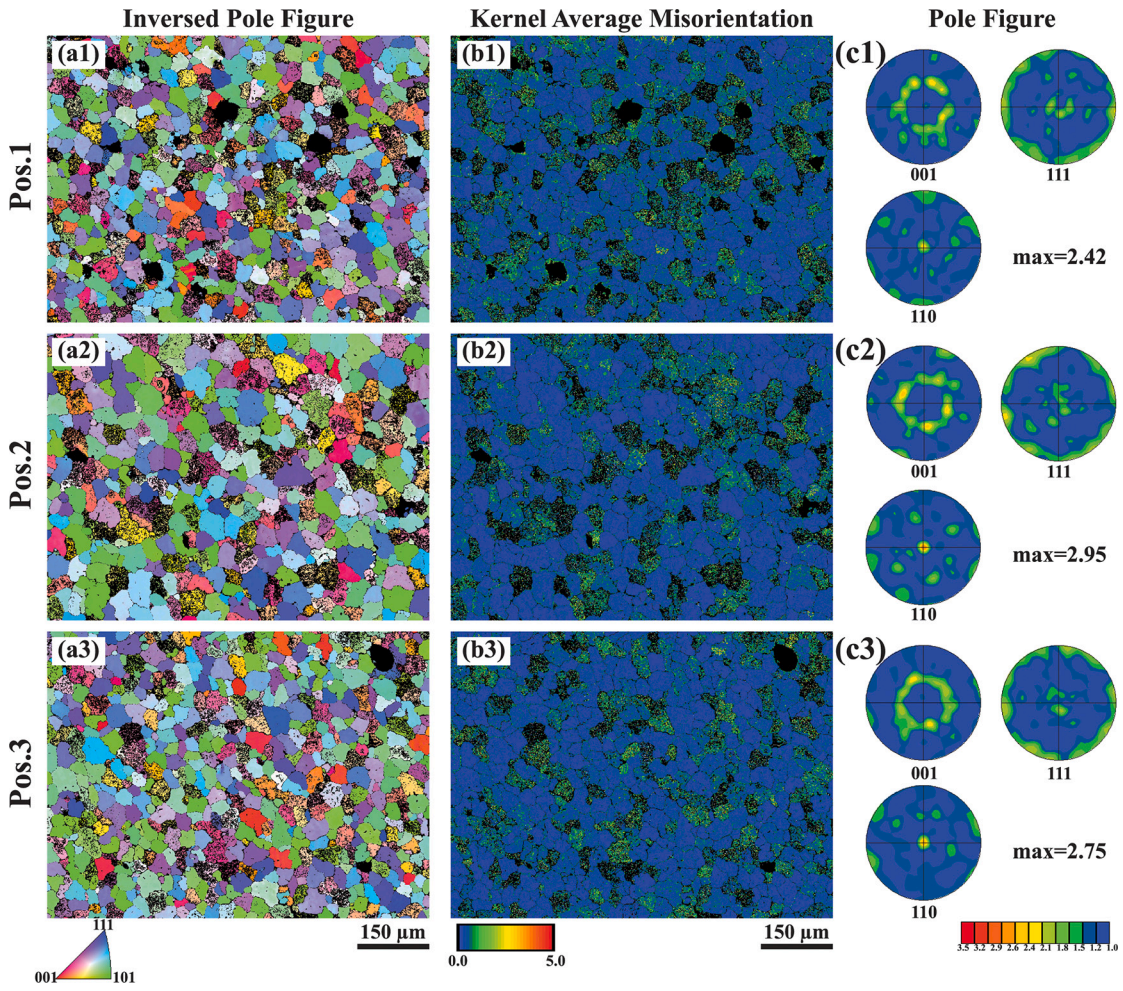

Fig. 9. EBSD maps showing (a1–3) IPF maps, (b1–3) KAM maps, and (c1–3) PF maps at different locations of deep UA sample.

the lower CI grain. In contrast, fewer nanoparticles were observed in the high CI grains. Therefore, the lower CI values are caused by preferential nanoparticle segregations within certain grains.

A larger area covering both the bright and dark etched region in the Surface UA sample is examined to investigate the relationship between CI values and grain orientation. CI value of 0.1 is generally considered as a threshold for successful indexing [39]. Fig. 8(a1–c1) show the IPF, KAM, and pole figs. (PF) maps of the data after rejecting the pixels with a CI value lower than 0.1. Data points with the CI values higher than 0.4 were reconstructed as the high CI partition, as shown in Fig. 8(a2–c2). Data points have a CI value between 0.1 and 0.4 were presented in the lower CI partition in Fig. 8(a3–c3). The KAM maps are highly correlated to the CI values as the lower CI pixels lead to incorrect orientation indexing as shown in Fig. 8(b), which introduces misleading local misorientations. Therefore, most of the high KAM grains exhibit lower CI values. However, one exceptional grain with both high KAM and CI value was spotted, as shown in Fig. 8(b2). This type of grain has been observed in additively manufactured components. The high KAM value is caused by high dislocation density [33,34], which is usually induced by repeated compression-tension cycles by the inhomogeneous thermal distribution in the sample [35] or nanoparticle blockage [36]. The grain with dense dislocations observed in this study is not likely induced by repeated deformation cycles since it is in the last layer of deposition. Considering the existence of TiB_2 nanoparticle in the weld wire, the theory that dislocation-dense grains form during solidification due to the difference in the thermal expansion coefficient of TiB_2 and aluminum matrix is more justifiable for this study.

A correlation between the CI value and orientation of grains can be observed, as shown in Fig. 8(c1, c2, and c3). For all the grains with CI values higher than 0.1, a texture in (110) is observed, as shown in Fig. 8 (c1), indicating a preferred epitaxial growth orientation during the solidification process. Fig. 8(c2) reveals a stronger texture in (110) in the high CI partition grains, while more random orientations were found in the lower CI partition (see Fig. 8(c3)). The (110) grains, which are also the preferred orientation for epitaxial grain growth, are associated with higher CI values. The grain map from TEM analysis by Lin et al. [28] also showed similar trend that (110) grains were better indexed than grains in other orientations.

The correlation between CI values and grain orientation can be attributed to the matrix-nanoparticle interactions. As a grain refiner, TiB_2 has a high-coherency orientation relationship (OR) with the α-Al, making it highly potent for heterogeneous nucleation during solidification. The OR of nucleation of α-Al on TiB_2 is [40,41]:

$$(0001)_{TiB_2} \| (111)_{Al}$$

$$[11\bar{2}0]_{TiB_2} \| [\bar{1}10]_{Al}$$

In the case of nanoparticle induced heterogeneous nucleation, the particles are located individually inside of α-Al grain. However, only a small percentage of nanoparticles are involved in the nucleation process. The majority is either pushed or engulfed by the solidification front. Based on our previous work, considerable amount of TiB_2 nanoparticles were clustered along the grain boundaries and secondary phases, indicating a strong pushing effect [24]. In this study, nanoparticles were also observed within the grains as in Fig. 7(c) and (d) via high-resolution BSE

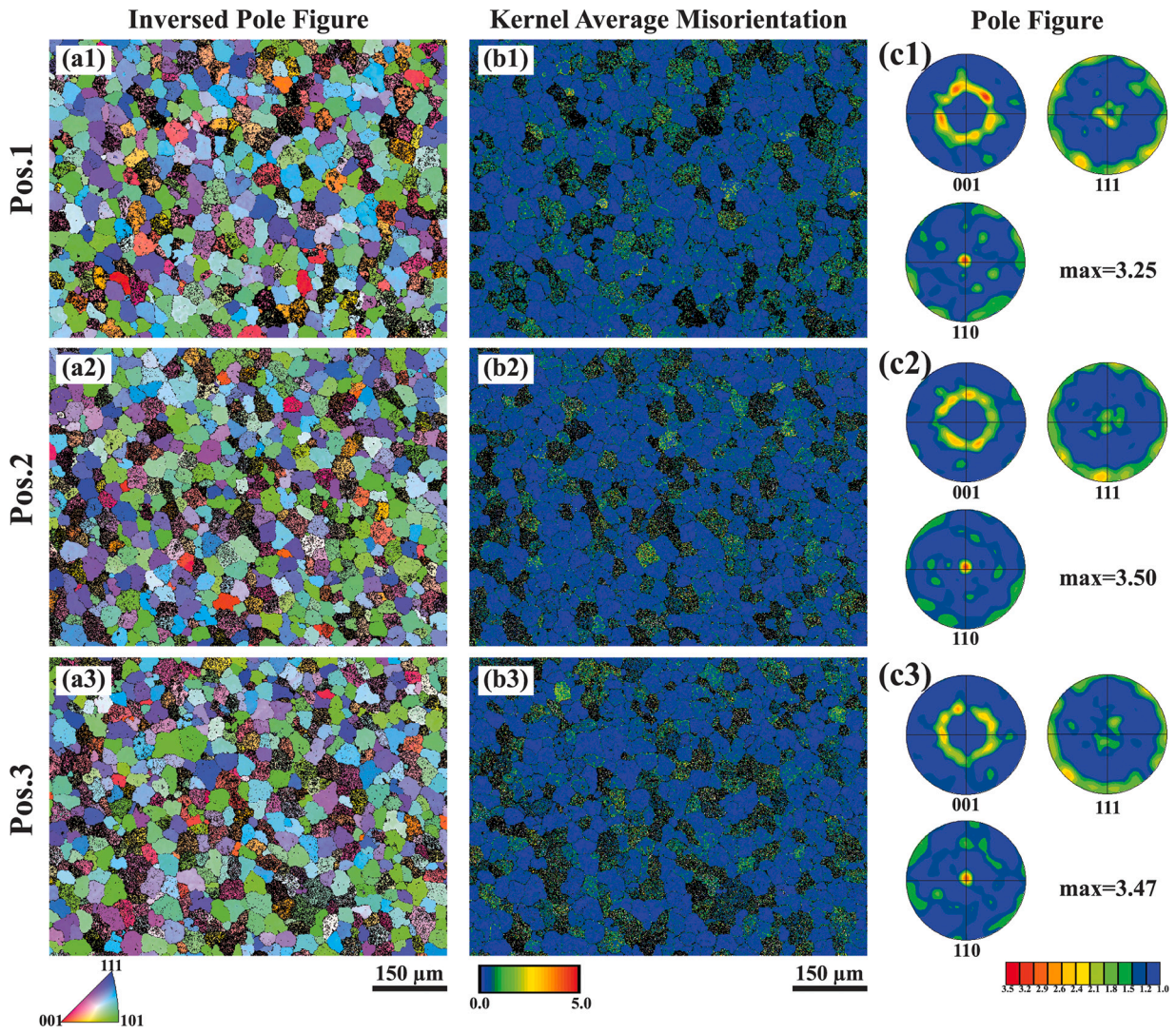

Fig. 10. EBSD maps showing (d1–3) IPF maps, (e1–3) KAM maps, and (f1–3) PF maps at different locations of no UA sample.

analysis, which were either engulfed nanoparticles or primary nucleation sites. Two major ORs of engulfed TiB_2 and α-Al determined in literature are as follows [42]:

OR1

$$(0001)_{TiB_2} \| (111)_{Al}$$

$$[11\bar{2}0]_{TiB_2} \| [\bar{1}10]_{Al}$$

OR2

$$(0001)_{TiB_2} \| (001)_{Al}$$

$$[2\bar{1}\bar{1}0]_{TiB_2} \| [110]_{Al}$$

where OR1 is the same as the OR for nucleation. OR1 and OR2 relationships indicate that the nanoparticles tend to be engulfed in (001) and (111) grains. Higher tendency of nanoparticle engulfment in these orientations leads to nanoparticles segregation, which interferes with the EBSD Kikuchi lines and induces relatively lower CI values, as discussed above. This also agrees with the observations of the strong (110) texture in high CI partition, since (110) grains are not favorable for either nanoparticle engulfment or heterogeneous nucleation.

EBSD analysis was further performed at three locations in Deep UA and No UA segments to investigate the UA effect on nanoparticle dispersion and grain orientations. These three locations are highlighted by white boxes in Fig. 2(b). Position 1 and 2 are at the top and bottom along the bead centerline, and Position 3 is in the middle part near the side surface of the bead. The results are shown in Figs. 9 and 10. More low CI grains can be found in the No UA condition than the Deep UA sample at all three locations. Considering the relationship between CI values and the nanoparticle distribution, the UA sample yields a better dispersion of nanoparticles while the No UA is more prone to nanoparticle segregations. Table 2 compares the area fraction of lower CI grains from the EBSD scanned maps. The average area fraction of lower CI grains in No UA sample is 22.7 %, which is higher than the 18.8 % in Deep UA sample. Besides, a (110) texture can be observed in all samples. As shown in Figs. 9(c) and 10(c), the texture intensities in Deep UA sample are 2.42, 2.95, and 2.75 at position 1, 2, and 3, respectively. In contrast, the corresponding texture intensities in No UA samples are

Table 2
Area fraction of grains with CI values from 0.1 to 0.4.

Position	No UA	Deep UA
1	19.4 %	19.3 %
2	23.3 %	18.8 %
3	25.4 %	18.2 %
Average	22.7 %	18.8 %

3.25, 3.50, and 3.47, respectively. Therefore, the Deep UA condition exhibits a weakened texture in (110). This could be induced by the multiple nonlinear UA effects on solidification. The acoustic streaming and cavitation can induce dendrite fragmentation, which suppresses preferential growth of (110) grains and promotes the development of more (001) and (111) grains.

During solidification, the (110) grains outgrow the grains in other orientations due to preferred epitaxial growth. On the other hand, the (110) grains are less favorable for nanoparticle engulfment, pushing the nanoparticles into (001) and (111) grains. In the no UA condition, the textured (110) grains lead to a stronger pushing effect of nanoparticles and result in segregation of nanoparticles in the limited number of (001) and (111) grains. Such segregations introduce overlaid Kikuchi patterns and cause lower CI values in the EBSD maps. In contrast, the Deep UA condition suppresses the (110) texture, which provides more preferrable grains for nanoparticle engulfment. Consequently, the nanoparticles can be distributed more uniformly. Furthermore, the UA-generated acoustic cavitation, streaming, and capillary effect directly enhances the dispersion of nanoparticles, which reduces the nanoparticle segregations in the (001) and (111) grains and accordingly the number of lower CI grains in the EBSD maps.

4. Conclusion

The UA effect on eutectic phase distribution, grain orientation, and nanoparticle dispersion at various probe positions in the Gas Tungsten Arc wire AM process at high deposition rate was studied with in situ high-speed imaging and post-mortem microstructure analysis. Main conclusions are the followings:

a) A deeper immersed UA probe generates faster acoustic streaming flow and stronger UA-melt interaction. With the UA probe placed on the melt pool surface, a bi-model microstructure forms, incorporating features from both No UA and deep UA conditions.
b) Immersing the UA probe deeper into the melt pool results in the formation of a more homogeneous microstructure with reduced eutectic phase at the grain boundaries. UA-enhanced mixing effect in the melt promotes the redistribution of solute atoms at the S/L interface and leads to delayed formation of eutectic phase.
c) Kikuchi line maps from EBSD analysis and high-resolution BSE imaging reveal that the lower CI grains are associated with the segregated intragranular nanoparticles. High CI grains exhibit a strong (110) texture, which has less favorable orientation relationships with engulfed nanoparticles.
d) UA results in a weaker (110) texture and a more randomly oriented grain structure with higher fraction of (001) and (111) grains, which are favorable for the homogeneous distribution of nanoparticles.

The ultrasonically assisted WAAM process can be applied to various types of materials that undergo multiple phase transformations during the solidification process, such as steels, titanium, and high entropy alloys and for fabrication of functional gradient materials. The current approach can be extended to Gas Metal Arc Welding (GMAW) based WAAM process which has different metal transfer modes. The UA effect under various metal transfer modes on the porosity, microstructure, and mechanical property could be further explored. The power ultrasound can be further applied to enhance different melt involved manufacturing processes in promoting refined and homogenized microstructure, such as fusion welding, casting, and other variants of additive manufacturing.

Declaration of competing interest

The authors declare that they have no known competing financial interests or personal relationships that could have appeared to influence the work reported in this paper.

Acknowledgement

This work is supported by National Science Foundation, CMMI AM Award # 2044526: CAREER: Ultrasonically Assisted Wire Arc Additive Manufacturing of Metal Matrix Nanocomposites for High-strength, Lightweight Structures. Electron microscopy was performed at the Center for Electron Microscopy and Analysis (CEMAS) at The Ohio State University. The authors acknowledge Dr. Jiarui Kang and Dr. Jianyue Zhang for their insightful discussion.

Appendix A. Supplementary data

Supplementary data to this article can be found online at https://doi.org/10.1016/j.jmapro.2023.09.043.

References

[1] Eskin GI. Broad prospects for commercial application of the ultrasonic (cavitation) melt treatment of light alloys. Ultrason Sonochem 2001;8:319–25. https://doi.org/10.1016/S1350-4177(00)00074-2.
[2] Eskin GI, Eskin DG. Ultrasonic Treatment of Light Alloy Melts. n.d.
[3] Yasui K. Acoustic cavitation and bubble dynamics. Cham: Springer International Publishing 2018. https://doi.org/10.1007/978-3-319-68237-2.
[4] Eskin GI. Cavitation mechanism of ultrasonic melt degassing. Ultrason Sonochem 1995;2:S137–41. https://doi.org/10.1016/1350-4177(95)00020-7.
[5] Tzanakis I, Eskin DG, Georgoulas A, Fytanidis DK. Incubation pit analysis and calculation of the hydrodynamic impact pressure from the implosion of an acoustic cavitation bubble. Ultrason Sonochem 2014;21:866–78. https://doi.org/10.1016/j.ultsonch.2013.10.003.
[6] Tzanakis I, Xu WW, Eskin DG, Lee PD, Kotsovinos N. In situ observation and analysis of ultrasonic capillary effect in molten aluminium. Ultrason Sonochem 2015;27:72–80. https://doi.org/10.1016/j.ultsonch.2015.04.029.
[7] Xu H, Jian X, Meek TT, Han Q. Degassing of molten aluminum A356 alloy using ultrasonic vibration. Mater Lett 2004;58:3669–73. https://doi.org/10.1016/j.matlet.2004.02.055.
[8] Xu H, Han Q, Meek TT. Effects of ultrasonic vibration on degassing of aluminum alloys. Mater Sci Eng A 2008;473:96–104. https://doi.org/10.1016/j.msea.2007.04.040.
[9] Eskin D, Alba-Baena N, Pabel T, da Silva M. Ultrasonic degassing of aluminium alloys: basic studies and practical implementation. Mater Sci Technol 2015;31:79–84. https://doi.org/10.1179/1743284714Y.0000000587.
[10] Hunt JD, Jackson KA. Nucleation of solid in an undercooled liquid by cavitation. J Appl Phys 1966;37:254–7. https://doi.org/10.1063/1.1707821.
[11] Eskin DG, Tzanakis I, Wang F, Lebon GSB, Subroto T, Pericleous K, et al. Fundamental studies of ultrasonic melt processing. Ultrason Sonochem 2019;52:455–67. https://doi.org/10.1016/j.ultsonch.2018.12.028.
[12] Tsunekawa Y, Suzuki H, Genma Y. Application of ultrasonic vibration to in situ MMC process by electromagnetic melt stirring. Materials & Design 2001;22:467–72. https://doi.org/10.1016/S0261-3069(00)00079-0.
[13] Kotadia HR, Qian M, Eskin DG, Das A. On the microstructural refinement in commercial purity Al and Al-10 wt% Cu alloy under ultrasonication during solidification. Materials & Design 2017;132:266–74. https://doi.org/10.1016/j.matdes.2017.06.065.
[14] Wang F, Eskin D, Mi J, Wang C, Koe B, King A, et al. A synchrotron X-radiography study of the fragmentation and refinement of primary intermetallic particles in an Al-35 Cu alloy induced by ultrasonic melt processing. Acta Mater 2017;141:142–53. https://doi.org/10.1016/j.actamat.2017.09.010.
[15] Li X, Yang Y, Cheng X. Ultrasonic-assisted fabrication of metal matrix nanocomposites. J Mater Sci 2004;39:3211–2. https://doi.org/10.1023/B:JMSC.0000025862.23609.6f.
[16] Eskin GI, Eskin DG. Production of natural and synthesized aluminum-based composite materials with the aid of ultrasonic (cavitation) treatment of the melt. Ultrason Sonochem 2003;10:297–301. https://doi.org/10.1016/S1350-4177(02)00158-X.
[17] Yang Y, Lan J, Li X. Study on bulk aluminum matrix nano-composite fabricated by ultrasonic dispersion of nano-sized SiC particles in molten aluminum alloy. Mater Sci Eng A 2004;380:378–83. https://doi.org/10.1016/j.msea.2004.03.073.
[18] Casati R, Vedani M. Metal matrix composites reinforced by nano-particles—a review. Metals 2014;4:65–83. https://doi.org/10.3390/met4010065.
[19] Kudryashova O, Vorozhtsov S. On the mechanism of ultrasound-driven deagglomeration of nanoparticle agglomerates in aluminum melt. JOM 2016;68:1307–11. https://doi.org/10.1007/s11837-016-1851-z.
[20] Rodrigues TA, Duarte V, Avila JA, Santos TG, Miranda RM, Oliveira JP. Wire and arc additive manufacturing of HSLA steel: effect of thermal cycles on microstructure and mechanical properties. Addit Manuf 2019;27:440–50. https://doi.org/10.1016/j.addma.2019.03.029.
[21] Williams SW, Martina F, Addison AC, Ding J, Pardal G, Colegrove P. Wire + arc additive manufacturing. Mater Sci Technol 2016;32:641–7. https://doi.org/10.1179/1743284715Y.0000000073.

[22] Todaro CJ, Easton MA, Qiu D, Zhang D, Bermingham MJ, Lui EW, et al. Grain structure control during metal 3D printing by high-intensity ultrasound. Nat Commun 2020;11:142. https://doi.org/10.1038/s41467-019-13874-z.
[23] Chen Y, Xu M, Zhang T, Xie J, Wei K, Wang S, et al. Grain refinement and mechanical properties improvement of Inconel 625 alloy fabricated by ultrasonic-assisted wire and arc additive manufacturing. J Alloys Compd 2022;910:164957. https://doi.org/10.1016/j.jallcom.2022.164957.
[24] Wang T, Mazánová V, Liu X. Ultrasonic effects on gas tungsten arc based wire additive manufacturing of aluminum matrix nanocomposite. Materials & Design 2022;214:110393. https://doi.org/10.1016/j.matdes.2022.110393.
[25] Wang T, Kang J, Darnell M, Liu X. Ultrasonically assisted hot-wire arc additive manufacturing process of AA7075 metal matrix nanocomposite. J Alloys Compd 2023;936:168298. https://doi.org/10.1016/j.jallcom.2022.168298.
[26] Greenwood MS, Mai JL, Good MS. Attenuation measurements of ultrasound in a kaolin–water slurry: a linear dependence upon frequency. J Acoust Soc Am 1993; 94:908–16. https://doi.org/10.1121/1.408192.
[27] Sokoluk M, Cao C, Pan S, Li X. Nanoparticle-enabled phase control for arc welding of unweldable aluminum alloy 7075. Nat Commun 2019;10:98. https://doi.org/10.1038/s41467-018-07989-y.
[28] Lin T-C, Cao C, Sokoluk M, Jiang L, Wang X, Schoenung JM, et al. Aluminum with dispersed nanoparticles by laser additive manufacturing. Nat Commun 2019;10: 4124. https://doi.org/10.1038/s41467-019-12047-2.
[29] Tang CY, Yang Z. Transmission Electron Microscopy (TEM). Membrane Characterization: Elsevier; 2017. https://doi.org/10.1016/B978-0-444-63776-5.00008-5. p. 145–59.
[30] Sokoluk M, Cao C, Pan S, Li X. Nanoparticle-enabled phase control for arc welding of unweldable aluminum alloy 7075. Nat Commun 2019;10:98. https://doi.org/10.1038/s41467-018-07989-y.
[31] Nakayama Y. Fundamentals of Flow. Introduction to Fluid Mechanics. Elsevier; 2018. p. 51–65. https://doi.org/10.1016/B978-0-08-102437-9.00004-8.
[32] Dong B, Cai X, Xia Y, Lin S, Fan C, Chen F. Effects of interlayer temperature on the microstructures of wire arc additive manufactured Al-Zn-Mg-Cu alloy: insights into texture responses and dynamic precipitation behaviors. Addit Manuf 2021;48: 102453. https://doi.org/10.1016/j.addma.2021.102453.
[33] Sokoluk M, Yuan J, Pan S, Li X. Nanoparticles enabled mechanism for hot cracking elimination in aluminum alloys. Metall Mater Trans A 2021;52:3083–96. https://doi.org/10.1007/s11661-021-06302-9.
[34] Ginsberg JH. Acoustics-a textbook for engineers and physicists: volume I: fundamentals. Cham: Springer International Publishing 2018. https://doi.org/10.1007/978-3-319-56844-7.
[35] Pierce AD. Acoustics: an introduction to its physical principles and applications. Cham: Springer International Publishing 2019. https://doi.org/10.1007/978-3-030-11214-1.
[36] Atamanenko TV, Eskin DG, Katgerman L. Melt Treatment, Grain Refinement & Modification I:Effects of Isothermal Ultrasonic Treatment on Microstructure of a Model Al-4wt% Cu Alloy. Aluminum Alloys. Their Physical and Mechanical Propertiesvol. 1. Aachen: Wiley-VCH GmbH & Co.; 2008. p. 315–20.
[37] Zhang L, Eskin DG, Miroux A, Katgerman L. Formation of microstructure in Al-Si alloys under ultrasonic melt treatment. In: Suarez CE, editor. Light metals 2012. Cham: Springer International Publishing; 2012. p. 999–1004. https://doi.org/10.1007/978-3-319-48179-1_174.
[38] Field DP. Recent advances in the application of orientation imaging. Ultramicroscopy 1997;67:1–9. https://doi.org/10.1016/S0304-3991(96)00104-0.
[39] Wright SI, Nowell MM, Lindeman SP, Camus PP, De Graef M, Jackson MA. Introduction and comparison of new EBSD post-processing methodologies. Ultramicroscopy 2015;159:81–94. https://doi.org/10.1016/j.ultramic.2015.08.001.
[40] Wang X, Song J, Vian W, Ma H, Han Q. The interface of TiB2 and Al3Ti in molten aluminum. Metall and Materi Trans B 2016;47:3285–90. https://doi.org/10.1007/s11663-015-0570-0.
[41] Qian P, Tang Z, Yuan M, Xiang Y, Wang L. Microstructure and refinement mechanism of TiB_2/$TiAl_3$ in remelted Al-5Ti-1B system. Mater Sci Technol 2019; 35:1563–71. https://doi.org/10.1080/02670836.2019.1629526.
[42] Schaffer PL, Miller DN, Dahle AK. Crystallography of engulfed and pushed TiB2 particles in aluminium. Scr Mater 2007;57:1129–32. https://doi.org/10.1016/j.scriptamat.2007.08.009.